crystals

MDPI

Article

Effect of Mg Alloying on the Mechanical Properties and Phase Transformation of Lithium

Nicolás Amigo [1,*], Rodrigo Vargas-Osorio [2], Facundo Esquivel [3] and Gonzalo Gutiérrez [3]

[1] Departamento de Física, Facultad de Ciencias Naturales, Matemática y del Medio Ambiente, Universidad Tecnológica Metropolitana, Las Palmeras 3360, Ñuñoa, Santiago 7800003, Chile
[2] Instituto Universitario de Investigación y Desarrollo Tecnológico, Universidad Tecnológica Metropolitana, Santiago 8330383, Chile; rodrigo.vargaso@utem.cl
[3] Departamento de Física, Facultad de Ciencias, Universidad de Chile, Casilla 653, Santiago 8330015, Chile; facundo.esquivel@ug.uchile.cl (F.E.); gonzalogutierrez@uchile.cl (G.G.)
* Correspondence: namigo@utem.cl

Abstract

This work presents an atomistic investigation of the structural and mechanical properties of Li–Mg alloys with 5, 10, and 20 at.% Mg using Monte Carlo and Molecular Dynamics simulations, elastic constant calculations, and uniaxial tensile tests. Structural equilibration revealed that Mg species promote enhanced relaxation and a tendency to form B2-type ordering. The elastic constants showed that Mg primarily increases the longitudinal stiffness while the shear-related components remained nearly unchanged. Derived mechanical properties confirm this strengthening trend, and comparison with recent experimental data shows good qualitative agreement. Tensile tests showed composition-dependent deformation mechanisms: the 0 and 5 at.% Mg samples underwent complete BCC-to-FCC transformation accompanied by strong stress reduction, the 10 at.% Mg alloy exhibited a similar transition while preserving positive stresses, and the 20 at.% Mg alloy displayed an abrupt shear-band instability that interrupted the transformation. These results provide insights into the role of Mg as an element that enhances the structural stability and mechanical stiffness of Li-Mg alloys, supporting their improved performance as electrode materials.

Keywords: structural properties; mechanical properties; lithium; molecular dynamics

1. Introduction

Lithium–magnesium (Li-Mg) alloys have emerged as promising candidates for solid-state battery (SSB) electrodes due to their high energy density and remarkable solid solubility in the lithium-rich phase. Incorporating Mg into Li can prevent dendrite formation, enhance hardness and creep resistance, and tune energy cycles for better long-term performance [1–3]. These features are particularly relevant for solid-state systems, where mechanical stability and resistance to degradation strongly influence device safety and efficiency [4–6].

Most research on SSBs has focused on ion transport and the electrochemical stability of solid electrolytes. Comparatively, fewer studies have explored their mechanical behavior, even though it plays a crucial role as the strains driven by mass transport affect not only the solid electrolyte but also the electrodes [4,7–9]. The mechanical performance of different composite materials as electrodes has been investigated in the literature, revealing strong couplings between electrochemical cycling, deformation, and degradation. Studies on graphite and carbon-nanotube composite anodes have shown that repeated

Check for updates

Academic Editor: Raluca Mereu

Received: 12 December 2025
Revised: 28 December 2025
Accepted: 29 December 2025
Published: 30 December 2025

Copyright: © 2025 by the authors. Licensee MDPI, Basel, Switzerland. This article is an open access article distributed under the terms and conditions of the Creative Commons Attribution (CC BY) license.

lithiation–delithiation generates significant residual strains that increase as capacity fades, with substrate stiffness strongly influencing the biaxial strain state of the active layer [10]. Similar behavior has been reported for amorphous Li_xSi, where plasticity induced by lithiation allows the material to flow while remaining prone to fracture. Higher lithiation rates elevate the flow stress, demonstrating the strong strain-rate sensitivity of silicon anodes and the increased driving force for cracking under fast charging [11]. Strain evolution at the electrode scale has been characterized in graphite–$LiCoO_2$ composites, where multiscale measurements and simulations reveal anisotropic swelling, load-path formation, and stress localization that govern electrode-level deformation [12]. Cathode materials such as $LiMn_2O_4$ exhibit pronounced irreversible strain variations during early cycles, and the magnitude of strain has been shown to scale with capacity fade under high-rate operation, reflecting chemo-mechanical degradation of the electrode structure [13]. Recent studies have addressed mechano-electrochemical fields. In graphite electrodes, real-time optical imaging revealed nonlinear lithium concentration and strain gradients along the diffusion direction, demonstrating a strong spatial coupling between chemistry and deformation [14]. Complementary in-situ measurements further showed that graphite experiences tensile strain and compressive stress distributions that evolve with lithium concentration, driven by the competing effects of mechanical constraint and Li-dependent stiffening [15]. Additional tensile and compressive loading studies on anodes and cathodes revealed strong anisotropy and significant rate-dependent strengthening, providing key data for failure modeling [16,17]. The onset of fracture has been analyzed through phase-field and strain-gradient plasticity frameworks, which showed that plastic strain localizes at two-phase interfaces and crack tips in electrode particles, while gradient effects help suppress catastrophic crack propagation [18]. Mechanical heterogeneity is especially critical in high-capacity materials such as silicon anodes, where micro-CT and digital volume correlation techniques revealed highly uneven volumetric changes and internal displacement fields during cycling, with local displacements reaching tens of micrometers [19]. Additionally, strategies to mitigate degradation in layered and spinel compounds used in Li- and Na-ion electrodes showed that volume changes can be systematically controlled by modifying the electronic, ionic, or structural contributions to expansion, enabling the design of strain-reduced or strain-less materials [20]. Finally, anodes such as β-Ti_2O_5 illustrate how the crystal structure drives the mechanical and electrochemical behavior, which can be tuned to eventually enhance cycling stability and rate capability, offering alternative routes for achieving mechanically robust, long-life electrodes [21].

Li-Mg alloys have emerged as promising candidates for next-generation lithium-metal negative electrodes [2,3] due to their enhanced mechanical stability, tunable transport properties, and ability to mitigate interfacial degradation. First-principles studies have shown that Mg addition significantly alters the fundamental mechanical behavior of Li-rich alloys, modifying stacking-fault energies and dislocation mobility across a wide compositional range [22]. Ab initio molecular dynamics simulations further revealed that Li induces transitions from close-packed to BCC-like local atomic structures, affecting diffusion mechanisms and mixing thermodynamics through strong Li–Mg interactions [23]. Experimental investigations have demonstrated that Mg alloying can improve contact retention at solid–electrolyte interfaces and enhance electrode stability, particularly at moderate Mg concentrations [24]. Further studies of Mg-Li-Zn alloys have additionally shown that Li content governs microstructural evolution, texture development, and mechanical strengthening under processing conditions [25]. More recent works have confirmed that low Mg additions can increase stiffness, hardness, and resistance to creep while still maintaining moderate Li transport properties, enabling improved cycling performance in solid-state configurations [3]. These studies highlight the role of Mg as a stabilizing

alloying element in Li metal anodes and reinforce the relevance of atomistic analysis of mechanical and structural behavior in Li-Mg systems.

Molecular dynamics (MD) simulations have become a relevant tool to study the mechanical behavior of materials, as they offer detailed information of the deformation mechanisms, local stress evolution, and atomic-scale structural rearrangements that are often inaccessible experimentally. Furthermore, MD enables the correlation of macroscopic mechanical responses with the underlying atomic structure. This capability is particularly valuable to evaluate the mechanical integrity of electrodes since it plays a decisive role in long-term cycling stability. In this context, exploring Li–Mg alloys is of significant interest due to their potential capabilities as electrode materials for lithium batteries. Thus, the present study investigates the structural properties and mechanical behavior of Li–Mg alloys with 0, 5, 10, and 20 at.% Mg, performing tensile tests with MD to evaluate the effect of Mg content on the structural response under external loading.

2. Materials and Methods

Atomic interactions between Li-Mg species were modeled with the interatomic potential developed by Kim et al. This potential is capable of simulating pure Li as well as Li-Mg alloys [26]. MD simulations were carried out with the Large-scale Atomic/Molecular Massively Parallel Simulator (LAMMPS) v22Jul2025 [27,28].

A crystalline BCC Li sample with four different Mg concentrations was prepared, namely 0, 5, 10, and 20 at.% Mg, with dimensions of $11.2 \times 11.2 \times 11.2$ nm^3 and lattice parameter 0.35 nm. Random atomic replacements were performed to achieve the target concentrations. The crystalline structure was constructed with the [100], [010], and [001] directions oriented along the x-, y-, and z-direction, respectively. A hybrid Monte Carlo (MC) and MD approach was used to equilibrate the samples, with 50 swaps per 100 steps under the NPT ensemble at 100 K and zero pressure with periodic boundary conditions (PBCs) for 1 ns. This temperature was chosen to avoid thermal fluctuations during structural characterization. Here we note that the lattice parameter depends on the Mg content. However, although the same lattice parameter was initially assigned to all alloys, the combined MC–MD approach allows the lattice parameter to adjust naturally during equilibration. This equilibration procedure ensures that the final atomic configurations reflect energetically favorable local correlations between Li and Mg species, rather than an artificial totally random distribution, which would correspond to a non-equilibrium state of the alloy.

Uniaxial tensile tests were performed by scaling the atomic positions in the x-direction with a strain rate of 10^8 s^{-1}. PBCs were kept in the y- and z-directions, while the temperature was maintained at 100 K and the pressure at zero in both the y- and z-directions using the NPT ensemble. All simulations were carried out with an integration time step of 1 fs. Visualization and analyses were conducted with the Open Visualization Tool (OVITO) v3.14.1 [29].

3. Results

3.1. Structural Characterization

During preparation and equilibration of the Li-Mg alloys under the MC-MD approach, the per-atom potential energy was calculated to monitor the structural relaxation and convergence of the system as adopted in previous studies [30–32]. The results are shown in Figure 1a. The per-atom potential energy of the 0% at. Mg case is included for comparison purposes. The 5% at. Mg alloy exhibits no significant variations during the MC-MD procedure, and its per-atom potential energy is slightly lower than the pure Li counterpart. However, significant reduction of the per-atom potential energy is observed for the 10% at. and 20% at. Mg samples, achieving final values of -1.637 eV/atom and -1.642 eV/atom,

respectively. Additionally, the curve for the 10% at. Mg converges after ∼0.3 ns, while for the 10% at. Mg convergence occurs after ∼0.7 ns, which is expected due to the larger fraction of Mg content.

The Warren–Cowley parameters were calculated to inspect the degree of attraction and repulsion between Li-Mg species.

$$\alpha_{i,j} = 1 - \frac{P_{i,j}}{c_j}, \tag{1}$$

where $P_{i,j}$ is the probability to find a j-type atom around a i-type atom, and c_j is the concentration of a j-type atom in the sample. Positive values indicate repulsion, while negative values indicate attraction. Figure 1b shows the values for the 5, 10, and 20% at. Mg samples. Values close to zero are observed for Li-Li interactions, reflecting that the sample consists of a Matrix of Li atoms. A decreasing trend is observed for Li–Mg interactions as the Mg content increases, indicating that these species tend to cluster, in agreement with the B2 crystalline structure that is formed when Li and Mg are present in equiatomic proportions [1,33]. Lastly, large positive values are observed for Mg–Mg interactions, indicating that Mg atoms tend to repel each other.

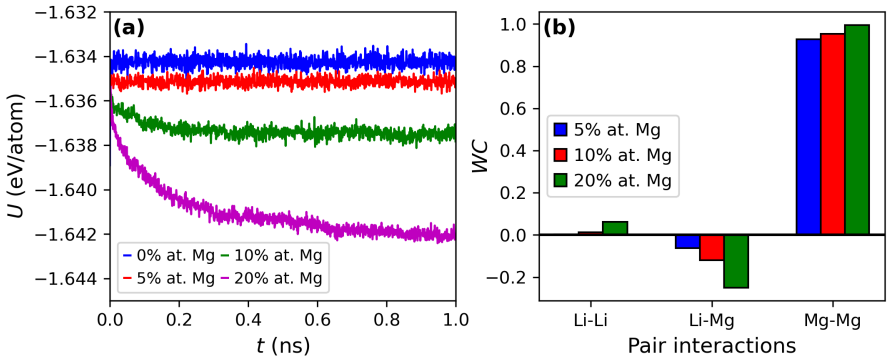

Figure 1. (**a**) Per-atom potential energy variation during the Monte Carlo and Molecular Dynamics simulations to equilibrate the Li-Mg alloys. (**b**) Warren–Cowley parameters for the Li-Li, Li-Mg, and Mg-Mg interactions.

Further characterization of the atomic structure was conducted through the radial distribution function. Figure 2a shows the results for the 0% at. Mg, that is, the pure Li sample. A strong peak is distinguished at 0.35 nm, corresponding to the lattice parameter for crystalline Li. Additional peaks are observed at larger distances, reflecting the medium-range and long-range order of the BCC crystalline structure. Partial radial distribution functions were also computed to inspect Li-Li, Li-Mg, and Mg-Mg interactions, resulting in the curves shown in Figure 2b–d. The overall shapes of the Li–Li, Li–Mg, and Mg–Mg curves are similar. However, the intensities of the first and second Mg–Mg peaks vary remarkably with Mg concentration. For the 5% at. Mg sample, the first Mg–Mg peak is very small, whereas the second peak is relatively large, indicating that Mg atoms tend to remain apart, consistent with their low concentration and the large available regions in the Li crystalline matrix that facilitate such separation. As the Mg content increases, the intensity of the first Mg–Mg peak increases, while the second peak decreases, reflecting a growing tendency for Mg atoms to be closer to one another due to the reduced availability of separated regions within the lattice.

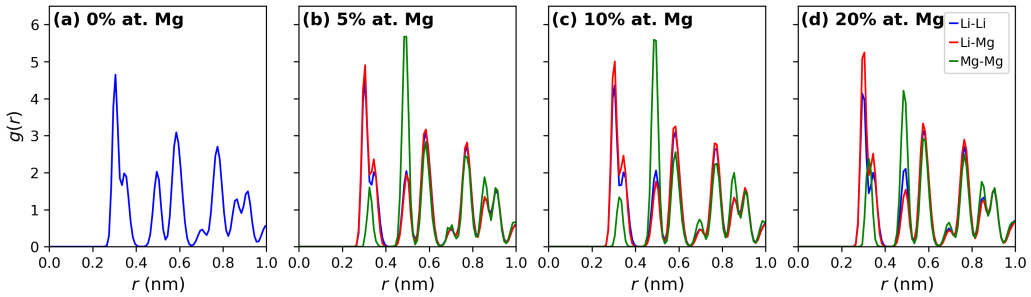

Figure 2. (**a**) Radial distribution function (g(r)) for the Li sample and (**b**) partial radial distribution functions for the (**b**) 5% at. Mg, (**c**) 10% at. Mg., and (**d**) 20% at. Mg.

3.2. Elastic Constants

Mechanical characterization was performed to shed light into the elastic response of the Li-Mg alloys. Figure 3 shows the variation of the stiffness tensor components and derived mechanical properties of Li–Mg alloys as a function of Mg content. As shown in Figure 3a, C_{11} increases with Mg addition, indicating that the alloy becomes stiffer against uniaxial deformation. In contrast, both C_{12} and C_{44} exhibit minor variations, indicating that the resistance to shear and lateral deformation remains almost the same across the different compositions under consideration. The mechanical properties were derived from the stiffness tensor components according to the following expression for an isotropic cubic metal

$$E = C_{11} - 2\nu C_{12}, \tag{2}$$

$$B = \frac{1}{3}(C_{11} + 2C_{12}), \tag{3}$$

$$G = C_{44}, \tag{4}$$

$$\nu = \frac{C_{12}}{C_{11} + C_{12}}, \tag{5}$$

where E is the Young's modulus, B the bulk modulus, G the shear modulus, and ν the Poisson's ratio. The resulting values are presented in Figure 3b. Here E increases with Mg concentration, in agreement with the rise of C_{11}, while G remains nearly constant, reflecting the weak dependence of C_{44} on Mg addition. The bulk modulus (B) shows a slight increase with Mg content, indicating a modest enhanced in resistance to volumetric compression. In contrast to E, the Poisson's ratio decreases monotonically with Mg, a behavior also observed for other metals materials [34,35]. These results indicate that Mg species strengthens the alloy primarly through an increase in longitudinal stiffness, while shear-related properties remain mostly insensitive to the atomic composition. A summary of the calculated values is presented in the Supplementary Material.

Experimental values for the stiffness tensor components for Li-Mg have been recently reported by Aspinall et al. [3]. Table 1 presents a comparison between those experimental values and the results obtained in this work, where the percentage difference is also shown. The trends in C_{11}, C_{12}, and C_{44} are in the same order of magnitude between both studies, although quantitative differences do exist. For C_{11}, deviations below 12% for 0 and 5 at.% Mg are observed, but differences increase at higher concentrations, reaching ~22% for the 20 at.% sample. In contrast, C_{12} exhibits good agreement for the 0 at.% Mg case, but it presents increasingly larger deviations with larger Mg contents, indicating that the alloying effect on lateral stiffness is underestimated by the interatomic potential. A similar behavior is observed for C_{44}, where deviations are below 1% for 5 at.% Mg, but increase up to 33% for the 20 at.% Mg case. These differences may arise from factors such as temperature effects, microstructural features, or limitations of the interatomic potential. Nonetheless, the comparison indicates that the employed potential captures the correct qualitative

trends and provides reasonable quantitative predictions, particularly at low to moderate Mg contents.

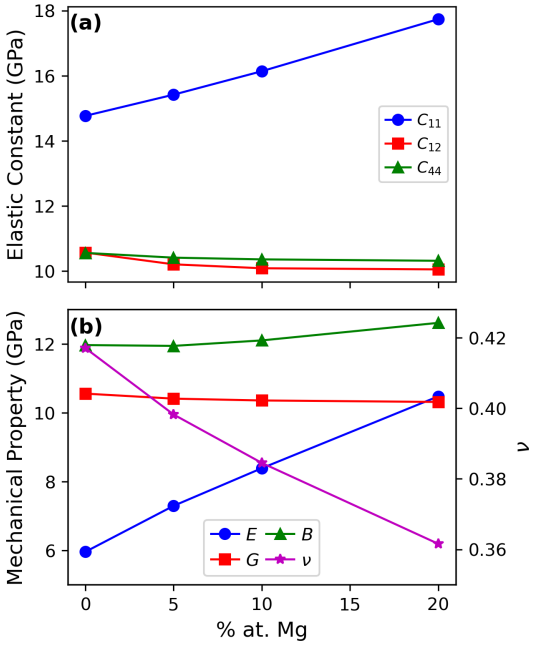

Figure 3. (**a**) Elastic constants and (**b**) derived mechanical properties for each Li-Mg alloy.

Table 1. Comparison of the stiffness tensor components obtained here and those reported by Aspinall et al. [3].

Constant	% at. Mg	This Work	Aspinall et al.	Difference (%)
C_{11}	0	14.8	13.3	11.3
	5	15.4	15.3	0.65
	10	16.1	19.2	16.1
	20	17.7	22.8	22.4
C_{12}	0	10.6	11.2	5.36
	5	10.2	13.2	22.7
	10	10.1	16.6	39.2
	20	10.0	19.7	49.2
C_{44}	0	10.6	8.8	20.4
	5	10.4	10.3	0.97
	10	10.4	13.0	20.0
	20	10.3	15.4	33.1

3.3. Uniaxial Tensile Tests

Uniaxial tensile tests were performed to evaluate the mechanical response of the Li-Mg alloys under external loading. Figure 4a shows the strain–stress curves for each composition. All samples exhibit a linear elastic regime up to ∼0.02 strain, followed by a maximum stress and then a drop in stress. Interestingly, the 0 at.% Mg and 5 at.% Mg samples exhibit negative values of σ_{xx} for strains above 0.10, whereas the 10 at.% Mg case displays a similar overall shape but with positive stress values. In contrast, the 20 at.% Mg sample shows an abrupt stress reduction at 0.145 strain, indicative of strong plastic deformation and a mechanical instability. To quantify these observations, the yield stress (σ_y) and maximum stress (σ_m) were calculated. σ_y was obtained using the 0.002 offset criterion, while σ_m was computed as the maximum stress of the curve. The resulting values are presented in Figure 4b. Both properties increase markedly with Mg concentration,

consistent with the enhanced stiffness and higher Young's modulus associated with Mg alloying discussed in the previous section. These trends highlight the strengthening effect of Mg additions, promoting greater resistance to deformation.

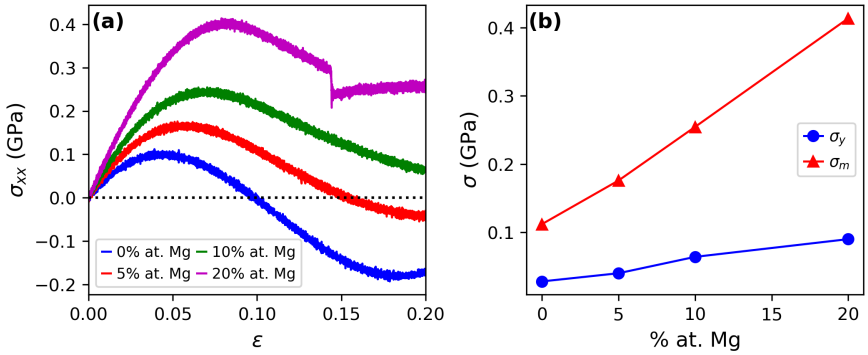

Figure 4. (**a**) Stress–strain curves for all the samples. The dotted black line denotes zero stress. (**b**) Yield stress (σ_y) and maximum stress (σ_m) calculated from the stress–strain curves.

To gain insights into the deformation behavior of the samples, the Polyhedral Template Matching (PTM) algorithm [36] was employed to analyze the crystalline structure. Figure 5 shows the structural evolution of the samples at different strains during the tensile tests. The negative stress values observed in the stress–strain curves occur at 0.10 and 0.15 strains for the 0 at.% and 5 at.% Mg samples, respectively, indicating that the FCC phase is more stable than the BCC phase. Then, both samples undergo a complete phase transformation from the BCC to the FCC structure. The 10 at.% Mg alloy exhibits a similar transformation, but maintains positive stress values throughout the test. From these observations, Mg atoms act as stabilizers of the BCC structure. Interestingly, the 20 at.% Mg sample displays a different behavior: although part of the BCC lattice begins to transform into FCC, a shear-band–like deformation occurs abruptly at a strain of 0.145, interrupting the transformation process.

While a direct BCC-to-FCC transformation has not been experimentally reported for lithium, previous studies have shown a two-step martensitic transformation from BCC to 9R and then to FCC at 95 K and 0.65 GPa [37–39]. These conditions are similar to those used in this work, supporting the capability of the interatomic potential to reproduce such structural transitions, in close agreement with previous reported phase diagrams for pure Li [40]. Additional studies have demonstrated that, depending on temperature and pressure, the FCC phase can be thermodynamically more stable than the BCC phase [41], which is consistent with the negative stresses observed during the transformation to FCC structure in the 0 at.% and 5 at.% samples.

Quantification of the BCC and FCC structural populations was performed during the tensile tests, resulting in the curves shown in Figure 6. In all cases, the BCC population decreases as the sample undergoes deformation, while the FCC population rapidly increases, reflecting the phase transformation. For the 0 at.%, 5 at.%, and 10 at.% Mg samples, an almost complete transformation is observed, with the intersection of BCC and FCC populations occurring at similar strains. However, a different scenario is observed for the 20 at.% Mg sample. In this case, although a full BCC-to-FCC transformation initially occurs, a rapid reverse transformation from FCC to BCC is distinguished, accompanied by the formation of unidentified and HCP structures. This behavior corresponds to the formation of shear-band–like features observed in Figure 5d. The sudden reverse transformation is likely attributable to an artifact of the interatomic potential due to the abrupt change of populations.

To better capture the deformation mechanisms observed at the experimental scale, future work should consider the use of interatomic potentials specifically optimized for

phase stability and deformation properties in Li–Mg systems, as well as simulations of polycrystalline models with realistic grain boundaries. In addition, lower strain rates, alternative deformation modes, and temperature conditions closer to experiments would further improve the predictive capability of the simulations.

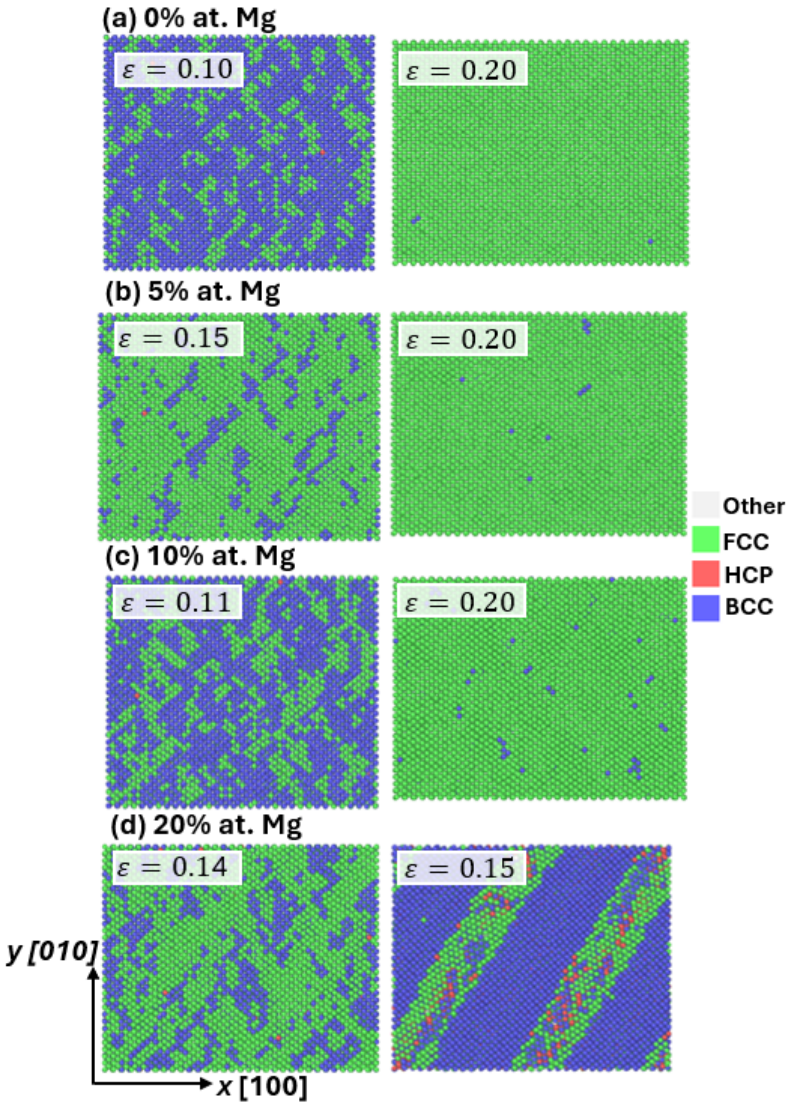

Figure 5. Phase transformation and deformation of the samples during the tensile tests. Atoms are colored according to the PTM algorithm: blue corresponds to BCC structure, green to FCC, red to HCP, and white to unidentified structure.

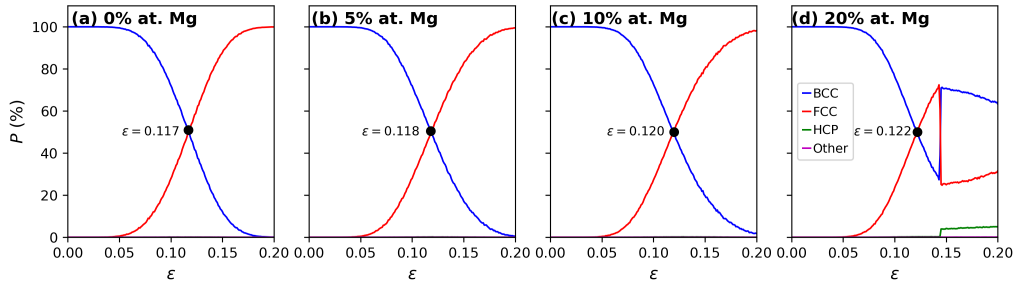

Figure 6. Variation of BCC, FCC, HCP and unidentified structure (label as *Other*) during the tensile tests. The black dot represents the intersection between the BCC and FCC curves. Atomic structure was inspected with the PTM algorithm.

4. Discussion

The tendency of the 0 and 5 at.% Mg samples to transform into an FCC structure exhibiting negative stresses, indicates that, under the simulated thermomechanical conditions, FCC becomes energetically more favorable than BCC. This behavior may manifest earlier when higher temperatures are considered, which are more relevant to practical applications. Such phase transformations align with experimental evidence showing that lithium can transition from BCC to close-packed phases at low temperatures and moderate pressures [37–39]. Although the intermediate 9R phase is not captured here, the simulations demonstrate that the interatomic potential qualitatively reproduces the thermodynamic driving forces associated with these transformations.

It has been reported that both deformation response and phase transformation is also influenced by the loading direction [42,43] and atomic composition [44,45]. While Mg species promoted enhanced stiffness which could be beneficial to suppress morphological instabilities at the electrode surface, shear instability and phase transformation are strongly dependent on loading orientation and stoichiometry. Therefore, it is crucial to explore these parameters to unveil alternative mechanisms or transformation sequences. Additionally, Li–Mg alloys are typically polycrystalline, containing grain boundaries that can promote or hinder phase transformation, act as nucleation sites for defects, and modify Mg distribution. Studying polycrystalline samples in future simulations would provide a more realistic representation of mechanical behavior, capturing microstructural effects absent in idealized single-crystal models.

Finally, the interatomic potential introduces some limitations that must be acknowledged. While it reproduces the qualitative trends in elastic and mechanical properties [3,46], quantitative deviations from experimental stiffness tensor components become increasingly pronounced, particularly for C_{12} and C_{44} at 10 at.% and 20 at.% Mg. This indicates that the potential likely underestimates alloying effects on lateral and shear-related elastic responses. In addition, the absence of the experimentally reported intermediate phases during transformation further suggest an incomplete description of the energy landscape. Future work should test different crystallographic orientations, explore polycrystalline samples, as well as perform simulations across a wider range of temperatures and atomic compositions.

5. Conclusions

This study provides an atomistic analysis of the structural and mechanical behavior of Li–Mg alloys with 5, 10, and 20 at.% Mg. The hybrid Monte Carlo and Molecular Dynamics equilibration revealed that increasing Mg content promotes stronger structural relaxation and a greater tendency for Mg atoms to cluster, consistent with the expected B2 ordering at higher concentrations. The stiffness tensor components and derived mechanical properties show that Mg additions strengthen the alloy by increasing the longitudinal stiffness, while shear-related properties remain nearly insensitive to composition. Comparison with experimental results demonstrates that the interatomic potential captures the qualitative trends, though quantitative deviations are significant. Uniaxial tensile tests revealed composition-dependent deformation mechanisms, including partial and complete BCC-to-FCC phase transformations, and a shear-band instability for the Mg-rich alloy.

Overall, the results highlight the effect of Mg incorporation on the deformation behavior of Li–Mg alloys. The simulations clarify the phase-transformation and the strengthening role of Mg, which is of particular relevance for lithium-battery electrodes: Mg enhances mechanical stability and increases stiffness, which could eventually mitigate issues such as surface roughening or dendritic growth in Li-based anodes. These findings provide a foundation of the atomistic origins of the mechanical behavior of Li–Mg alloys as candidates for next-generation lithium metal electrodes. Future work should extend this analysis to

polycrystalline samples, alternative loading orientations, different atomic compositions, and varying temperatures to explore their effect on Li-Mg alloys.

Supplementary Materials: The following supporting information can be downloaded at: https://www.mdpi.com/article/10.3390/cryst16010031/s1, Table S1: Calculated elastic constants in this work through molecular dynamics simulations.

Author Contributions: N.A.: Conceptualization, Software, Methodology, Supervision, Formal analysis, Writing—review & editing—original draft, Resources. R.V.-O.: Formal analysis, Visualization. F.E.: Formal analysis. G.G.: Conceptualization, Writing—review & editing. All authors have read and agreed to the published version of the manuscript.

Funding: Project supported by the Competition for Research Regular Projects, year 2023, code LPR23-05, Universidad Tecnológica Metropolitana. N.A. thanks to Fondo Nacional de Desarrollo Científico Tecnológico (FONDECYT, Chile) under grants #1251338 and #1251905. Powered@NLHPC: This research was partially supported by the supercomputing infrastructure of the NLHPC (ECM-02).

Data Availability Statement: The original contributions presented in this study are included in the Supplementary Materials.

Acknowledgments: During the preparation of this manuscript, the authors used ChatGPT-3.5 for the purposes of grammar and language checking. The authors have reviewed and edited the output and take full responsibility for the content of this publication.

Conflicts of Interest: The authors declare no conflicts of interest.

References

1. Taylor, R.H.; Curtarolo, S.; Hart, G.L.W. Ordered magnesium-lithium alloys: First-principles predictions. *Phys. Rev. B* **2010**, *81*, 024112. [CrossRef]
2. Lewis, J.A.; Cavallaro, K.A.; Liu, Y.; McDowell, M.T. The promise of alloy anodes for solid-state batteries. *Joule* **2022**, *6*, 1418–1430. [CrossRef]
3. Aspinall, J.; Sada, K.; Guo, H.; Kotakadi, S.; Narayanan, S.; Chart, Y.; Jagger, B.; Milan, E.; Brassart, L.; Armstrong, D.; et al. The impact of magnesium content on lithium-magnesium alloy electrode performance with argyrodite solid electrolyte. *Nat. Commun.* **2024**, *15*, 4511. [CrossRef]
4. Kalnaus, S.; Dudney, N.J.; Westover, A.S.; Herbert, E.; Hackney, S. Solid-state batteries: The critical role of mechanics. *Science* **2023**, *381*, eabg5998. [CrossRef]
5. Schmaltz, T.; Hartmann, F.; Wicke, T.; Weymann, L.; Neef, C., Janek, J. A Roadmap for Solid-State Batteries. *Adv. Energy Mater.* **2023**, *13*, 2301886. [CrossRef]
6. Joshi, A.; Mishra, D.K.; Singh, R.; Zhang, J.; Ding, Y. A comprehensive review of solid-state batteries. *Appl. Energy* **2025**, *386*, 125546. [CrossRef]
7. Kang, J.; Shin, H.R.; Yun, J.; Kim, S.; Kim, B.; Lee, K.; Lim, Y.; Lee, J.W. Chemo-mechanical failure of solid composite cathodes accelerated by high-strain anodes in all-solid-state batteries. *Energy Storage Mater.* **2023**, *63*, 103049. [CrossRef]
8. Kim, K.H.; Lee, M.J.; Ryu, M.; Liu, T.K.; Lee, J.H.; Jung, C.; Kim, J.S.; Park, J.H. Near-strain-free anode architecture enabled by interfacial diffusion creep for initial-anode-free quasi-solid-state batteries. *Nat. Commun.* **2024**, *15*, 3586. [CrossRef]
9. Xu, C.; Feng, J.; Sun, S.; Zhao, X. Designing low-strain cathode materials for long-life all-solid-state batteries. *J. Mater. Chem. A* **2024**, *12*, 14940–14956. [CrossRef]
10. Chen, J.; Thapa, A.K.; Berfield, T.A. In-situ characterization of strain in lithium battery working electrodes. *J. Power Sources* **2014**, *271*, 406–413. [CrossRef]
11. Pharr, M.; Suo, Z.; Vlassak, J.J. Variation of stress with charging rate due to strain-rate sensitivity of silicon electrodes of Li-ion batteries. *J. Power Sources* **2014**, *270*, 569–575. [CrossRef]
12. Rieger, B.; Schlueter, S.; Erhard, S.V.; Jossen, A. Strain Propagation in Lithium-Ion Batteries from the Crystal Structure to the Electrode Level. *J. Electrochem. Soc.* **2016**, *163*, A1595. [CrossRef]
13. Çapraz, Ö.Ö.; Rajput, S.; White, S.; Sottos, N.R. Strain Evolution in Lithium Manganese Oxide Electrodes. *Exp. Mech.* **2018**, *58*, 561–571. [CrossRef]
14. Yang, W.; Xie, H.; Shi, B.; Song, H.; Qiu, W.; Zhang, Q. In-situ experimental measurements of lithium concentration distribution and strain field of graphite electrodes during electrochemical process. *J. Power Sources* **2019**, *423*, 174–182. [CrossRef]

15. Xie, H.; Han, B.; Song, H.; Li, X.; Kang, Y.; Zhang, Q. In-situ measurements of electrochemical stress/strain fields and stress analysis during an electrochemical process. *J. Mech. Phys. Solids* **2021**, *156*, 104602. [CrossRef]
16. Sonwane, A.; Yuan, C.; Xu, J. Coupling Effect of State-of-Charge and Strain Rate on the Mechanical Behavior of Electrodes of 21700 Lithium-Ion Battery. *J. Electrochem. Energy Convers. Storage* **2020**, *18*, 020905. [CrossRef]
17. Li, H.; Gu, J.; Zhou, D.; Cui, Z.; Li, P.; Zhang, C. Rate-dependent damage and failure behavior of lithium-ion battery electrodes. *Eng. Fract. Mech.* **2024**, *303*, 110143. [CrossRef]
18. Xue, R.; Li, X.; Zhao, H.; Chen, Z. Phase field model coupling with strain gradient plasticity for fracture in lithium-ion battery electrodes. *Eng. Fract. Mech.* **2022**, *269*, 108518. [CrossRef]
19. Wang, B.; Xue, K.; Xi, L.; Chen, H.; Wen, J.; Ma, C.; Li, Y. Enhanced strain mapping Unveils internal deformation dynamics in Silicon-based lithium-ion batteries during electrochemical cycling. *Mater. Des.* **2024**, *247*, 113404. [CrossRef]
20. Maréchal, M.; Berthelot, R.; Rozier, P.; Saubanère, M. Designing Strain-Less Electrode Materials: Computational Analysis of Volume Variations in Li-Ion and Na-Ion Batteries. *Batteries* **2024**, *10*, 262. [CrossRef]
21. Li, X.; Zhang, J.; An, X.; Liu, Q.; Xie, L.; Yao, W.; Kong, Q. Crystal structure regulation of trititanium pentoxide for advanced zero-strain lithium storage anode. *J. Colloid Interface Sci.* **2025**, *678*, 566–574. [CrossRef]
22. Shin, I.; Carter, E.A. First-principles simulations of plasticity in body-centered-cubic magnesium–lithium alloys. *Acta Mater.* **2014**, *64*, 198–207. [CrossRef]
23. Wang, J.; Zhang, Q.; Qin, J. Structural transition region of liquid Mg–Li alloys. *Comput. Mater. Sci.* **2016**, *117*, 259–265. [CrossRef]
24. Krauskopf, T.; Mogwitz, B.; Rosenbach, C.; Zeier, W.G.; Janek, J. Diffusion Limitation of Lithium Metal and Li–Mg Alloy Anodes on LLZO Type Solid Electrolytes as a Function of Temperature and Pressure. *Adv. Energy Mater.* **2019**, *9*, 1902568. [CrossRef]
25. Ji, H.; Wu, G.; Liu, W.; Liang, X.; Liao, G.; Ding, D. Microstructure characterization and mechanical properties of the as-cast and as-extruded Mg-xLi-5Zn-0.5Er (x = 8, 10 and 12 wt%) alloys. *Mater. Charact.* **2020**, *159*, 110008. [CrossRef]
26. Kim, Y.M.; Jung, I.H.; Lee, B.J. Atomistic modeling of pure Li and Mg–Li system. *Model. Simul. Mater. Sci. Eng.* **2012**, *20*, 035005. [CrossRef]
27. Plimpton, S. Fast Parallel Algorithms for Short-Range Molecular Dynamics. *J. Comput. Phys.* **1995**, *117*, 1–19. [CrossRef]
28. Thompson, A.P.; Aktulga, H.M.; Berger, R.; Bolintineanu, D.S.; Brown, W.M.; Crozier, P.S.; in 't Veld, P.J.; Kohlmeyer, A.; Moore, S.G.; Nguyen, T.D.; et al. LAMMPS—A flexible simulation tool for particle-based materials modeling at the atomic, meso, and continuum scales. *Comp. Phys. Comm.* **2022**, *271*, 108171. [CrossRef]
29. Stukowski, A. Visualization and analysis of atomistic simulation data with OVITO–the Open Visualization Tool. *Model. Simul. Mater. Sci. Eng.* **2010**, *18*, 015012. [CrossRef]
30. Amigo, N. Mechanical characterization of nanocrystalline Cu-Ag alloys subjected to shear deformation. *Mol. Simul.* **2024**, *50*, 1411–1419. [CrossRef]
31. Niu, Y.; Zhao, D.; Zhu, B.; Wang, S.; Zhang, Z.; Zhao, H. Research on the effects of chemical short-range order on strengthening and toughening mechanisms of FCC/BCC dual-phase high-entropy alloys at micro/nano-scale. *Mater. Today Commun.* **2024**, *41*, 111064. [CrossRef]
32. Samsonov, V.; Lutsay, A.; Zhigunov, D.; Puytov, V.; Romanov, A. Self-assembly of three-shell nanostructures in initially homogeneous binary metallic nanoparticles: Hybrid molecular dynamics/Monter-Carlo simulations. *Phys. B Condens. Matter* **2025**, *718*, 417898. [CrossRef]
33. Hafner, J.; Weber, W. Total-energy calculations for intermetallic compounds with a first-principles linear combination of atomic orbitals method. *Phys. Rev. B* **1986**, *33*, 747–754. [CrossRef] [PubMed]
34. Cui, Z.; Gao, F.; Cui, Z.; Qu, J. A second nearest-neighbor embedded atom method interatomic potential for Li-Si alloys. *J. Power Sources* **2012**, *207*, 150–159. [CrossRef]
35. Gunkelmann, N.; Ledbetter, H.; Urbassek, H.M. Experimental and atomistic study of the elastic properties of a Fe-C martensite. *Acta Mater.* **2012**, *60*, 4901–4907. [CrossRef]
36. Larsen, P.M.; Schmidt, S.; Schiøtz, J. Robust structural identification via polyhedral template matching. *Model. Simul. Mater. Sci. Eng.* **2016**, *24*, 055007. [CrossRef]
37. Smith, H.; Berliner, R.; Jorgensen, J. Martensitic transformation from BCC to 9R and FCC in metallic lithium. *Phys. B Condens. Matter* **1989**, *156–157*, 53–55. [CrossRef]
38. Smith, H.G.; Berliner, R.; Jorgensen, J.D.; Nielsen, M.; Trivisonno, J. Pressure effects on the martensitic transformation in metallic lithium. *Phys. Rev. B* **1990**, *41*, 1231–1234. [CrossRef]
39. Schwarz, W.; Blaschko, O. Polytype structures of lithium at low temperatures. *Phys. Rev. Lett.* **1990**, *65*, 3144–3147. [CrossRef]
40. Dorrell, J.; Pártay, L.B. Pressure–Temperature Phase Diagram of Lithium, Predicted by Embedded Atom Model Potentials. *J. Phys. Chem. B* **2020**, *124*, 6015–6023. [CrossRef] [PubMed]
41. Ackland, G.J.; Dunuwille, M.; Martinez-Canales, M.; Loa, I.; Zhang, R.; Sinogeikin, S.; Cai, W.; Deemyad, S. Quantum and isotope effects in lithium metal. *Science* **2017**, *356*, 1254–1259. [CrossRef]

42. Amini, H.; Simchi, A.; Kokabi, A. Effects of crystal orientation on the tensile and shear deformation of nickel–silicon interfaces: A molecular dynamics simulation. *Mater. Sci. Eng. A* **2012**, *543*, 217–223. [CrossRef]
43. Gao, Y.; Wang, H.; Zhao, J.; Sun, C.; Wang, F. Anisotropic and temperature effects on mechanical properties of copper nanowires under tensile loading. *Comput. Mater. Sci.* **2011**, *50*, 3032–3037. [CrossRef]
44. Jiao, Y.; Dan, W.; Zhang, W. The strain-induced martensitic phase transformation of Fe–C alloys considering C addition: A molecular dynamics study. *J. Mater. Res.* **2020**, *35*, 1803–1816. [CrossRef]
45. Amigo, N. NiTi shape memory alloys under nanoindentation with different atomic compositions. *Mol. Simul.* **2024**, *50*, 936–943. [CrossRef]
46. Trivisonno, J.; Smith, C.S. Elastic constants of lithium-magnesium alloys. *Acta Metall.* **1961**, *9*, 1064–1071. [CrossRef]

Disclaimer/Publisher's Note: The statements, opinions and data contained in all publications are solely those of the individual author(s) and contributor(s) and not of MDPI and/or the editor(s). MDPI and/or the editor(s) disclaim responsibility for any injury to people or property resulting from any ideas, methods, instructions or products referred to in the content.